Bidirectional Non-Isolated Fast Charger Integrated in the Electric Vehicle Traction Drivetrain

Michael Eull, *Student Member, IEEE*, Liwei Zhou, *Student Member, IEEE*, Matthew Jahnes, *Student Member, IEEE* and Matthias Preindl, *Senior Member, IEEE*

***Abstract*—Integrated chargers, where the traction inverter is used as the primary charging interface, have emerged as a solution for reducing the cost and footprint of electric vehicle charging. This paper proposes a bidirectional non-isolated integrated charger topology that also provides benefits to motor lifetime and reliability through a reduction in bearing currents and voltages. This is achieved by adding to an electric vehicle drive: an LC filter per phase with a common mode voltage control; a common mode inductor for additional leakage current filtering; contactors to switch between traction and charging modes; and a residual current device to satisfy standards for transformerless charging. To obtain high efficiency and make the filter small for traction applications, variable frequency critical soft switching is leveraged. Traction mode experimental validation demonstrates torque and speed steps with no degradation compared to a standard drive, a decrease in leakage currents and shaft voltages of more than 90% and an increase in motor drive efficiency of 0.6% at 5kW output power. Charging mode validation shows active and reactive power steps and peak efficiency of 99.4% and 98.4% at rated power of 11kW. Charging mode leakage current is measured to be 22mA, which satisfies standards permitting transformerless operation.**

***Index Terms*—Battery chargers, motor drives**

I. Introduction

Electric vehicles (EVs) are a promising avenue to reducing the substantial worldwide carbon footprint of transportation [1]. Key obstacles facing the widespread adoption of EVs are the costs of the vehicles themselves and the cost and availability of charging infrastructure. While overall costs are trending downwards as the underlying technologies advance [2] and researchers find ways to supplant hardware with software [3, 4, 5] for drives, the cost of chargers remains high. This has been recognized by the United States Department of Energy as a part of the "EV Everywhere Challenge," where technical targets have been outlined for the entire EV system, including on-board chargers. The on-board charger targets are listed in Table I, where a significant improvement in cost and power density are envisioned for accelerating EV proliferation [2].

Manuscript received March 31, 2021; revised June 22, 2021 and September 8, 2021; accepted October 18, 2021. This research was supported by National Science Foundation grant 1653574.

Michael Eull is with the Power Networks Demonstration Centre, University of Strathclyde, Glasgow G1 1XQ, United Kingdom (e-mail: michael.eull@strath.ac.uk).

Liwei Zhou, Matthew Jahnes and Matthias Preindl are with the Department of Electrical Engineering, Columbia University in the City of New York, New York, NY 10027, USA (e-mail: lz2575@columbia.edu; mhj2117@columbia.edu; matthias.preindl@columbia.edu).

Color versions of one or more of the figures in this paper are available online at http://ieeexplore.ieee.org.

TABLE I: United States Department of Energy on-board charger technical targets for 500,000 units [2].

On-Board Charger Targets	2020	2025
Cost ($/kW)	50	35
Specific power (kW/kg)	3	4
Power density (kW/L)	3.5	4.6
Efficiency	97%	98%

Significant research effort has been expended in designing chargers for electric vehicles [6], both low and high power, which can be unidirectional for EV charging only or bidirectional to provide grid services [7]. On-board discrete chargers are typically lower power to minimize the size and weight of added components [6], which limits charging rates. Off-board standalone charging units are typically higher power and capable of fast charging the vehicle [8]. A third class of chargers is referred to as *integrated*, where they are built into the drivetrain of the vehicle. Integrated chargers provide the opportunity to bring high power charging on-board the vehicle with minimal need of additional power electronics by reusing existing traction components. This reuse facilitates high power charging as traction drive power ratings are typically 30-60kW for hybrid EVs and 100+kW for battery EVs [9].

Because of the unique benefits integrated chargers present, they have gained the attention of the research and automotive communities [10, 11, 12], with Renault adopting the so-called "Chameleon inverter" integrated charger into production vehicles [13]. Integrated chargers typically fall into one of two categories [12]: the first uses electric machines with phase counts greater than three (herein referred to as *multi-phase*) due to issues surrounding the charging torque phenomenon; the second where additional power electronics are added to the drive, referred to as *add-on interfaces*. Regardless of classification, integrated chargers have two operating modes: *traction mode*, where the traction inverter drives the motor, and *charging mode*, where the traction inverter is used as the primary battery charging interface.

Multi-phase integrated chargers propose using the windings of electric machines with more than three phases to realize charging. Multi-phase integrated chargers previously studied in the literature include a five-phase induction machine (IM) [14], six-phase IM [15], nine-phase IM [16] and a six-phase permanent magnet synchronous machine (PMSM) [17, 18]. A special case of the multi-phase setup is the split-phase machine, which has been shown to be

effective for PMSMs [19, 20, 21] and IMs [22]. Depending on the distribution of the windings, split-phase machines can be isolated as well [19, 10]. Applying a sinusoidal voltage and current through the windings of the machine requires additional design and control to prevent charging torque generation that will cause the motor (and, hence, vehicle) to move during charging. Because charging is done with sinusoidal voltages and currents, bidirectional operation is possible but not often studied. A review of multi-phase integrated chargers and their special considerations is provided in [11].

Charging torque with integrated chargers using the traction machine's windings can be problematic due to the rotation of the machine, which will cause the shaft to move and vibrate. There have been numerous suggestions in the literature for how to defeat this challenge. The majority use multi-phase machines and some form of control algorithm. Other proposed solutions have been to shift the rotor to a non-torque generating position for a six-phase PMSM [18], to design the windings with a certain displacement to cancel torque [17], to add a clutch to disconnect the motor from the transmission during charging [19] or to reconfigure the system for traction and charging modes [10, 21, 22], which includes the Chameleon inverter in production vehicles [13].

Add-on interfaces cover integrated chargers that require some addition of power electronics to be realized, typically a rectifier for unidirectional operation or an inverter for bidirectional, as well as an EMI filter. Regardless of implementation, add-on interfaces convert the AC voltage from the grid to a DC quantity before using the three-phase inverter as DC/DC converter in charging mode. The two most popular implementations either require access to the neutral point of the machine [13, 23, 24, 25] or to one of the phase legs [26, 27, 28]. Another topology uses the inverter as a three-phase buck/boost converter with the motor windings acting as the inductor [29]. In the case of a switched reluctance machine, the inverter topology makes it possible to unidirectionally charge without added components [30].

Multi-phase and add-on interface integrated chargers each have their own respective benefits and drawbacks. The major benefits of multi-phase topologies are that they are able to realize bidirectional charging most easily, can be made isolated by design or application of the machine and requiring no additional power electronics for the sole purpose of charging. Drawbacks of multi-phase implementations are that they require electric machines with phase counts greater than three, which is not ideal as three-phase machines have become the norm for electrified transportation applications [12], that additional power electronics will still be required regardless due to the need to drive the additional phases and the need to implement charging torque cancellation algorithms. Benefits of add-on interfaces are that three-phase machines are not a problem and neither is charging torque due to passing DC current through the windings or bypassing them entirely. The biggest drawback of an add-on interface is that additional power electronics and EMI filters for rectification are necessary due to the AC to DC conversion process. For high power charging, the rectifier and EMI filter could become large, which is not advantageous for being on-board the EV.

Another difficulty in bringing high power charging on-board is the need to have a transformer to keep the leakage current at safe levels. Per IEC [31, 32] and IET [33] standards, the leakage current needs to remain below 30mA for human safety. Generated by the fluctuation of the common mode voltage that switched inverters generate, the simplest way to become compliant is to add a transformer, typically with a high frequency transformer for on-board chargers or a line frequency transformer for charging stations. However, high power transformers can be large, costly and inefficient, making high power on-board charging difficult to achieve.

Transformerless topologies have become popular in photovoltaic applications [34], though they normally increase converter complexity through additional transistors and diodes (i.e. multi-level converters). The same is true for automotive applications [35]. Recent photovoltaic and automotive research has shown zero sequence/common mode voltage control to be effective for the elimination of the leakage current in single- [36, 37] and three-phase [38] grid interfaces, where an LC filter per phase with the filter capacitor connected to the DC negative is introduced along with an additional control stage. Removing the transformer can lead to a system efficiency increase that is not normally discussed in the literature, meaning that the additional losses presented by the LC filter and larger current ripple through the transistors can be offset. Also, the LC filter is capable of providing reactive power to replace the extra power factor correction (PFC) circuit and inductors. Thus, the cost can be further saved.

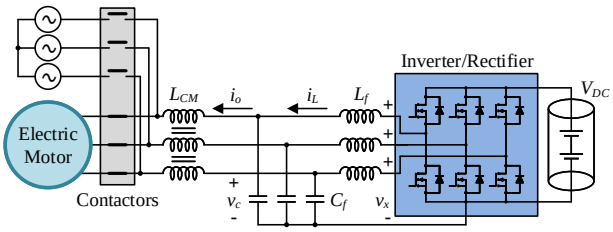

Fig. 1: Proposed integrated charger using contactors to change between traction and charging modes.

Despite the difficulties integrated charging poses, it remains an attractive option for advancing electric vehicle adoption. This paper proposes a bidirectional non-isolated integrated charger topology. To realize this, a few components must be added to the traction drive. They are: an LC filter per phase with a common mode voltage control [38]; a common mode (CM) inductor for additional leakage current filtering; contactors to switch between traction and charging modes; and a residual current device (RCD) to satisfy standards for transformerless charging. The implementation studied uses contactors to switch between operation modes to avoid the difficulties associated with

charging torque and to keep efficiency in charging mode as high as possible. An alternate configuration using an open-winding machine is possible with an appropriate charging torque cancellation scheme. Focus is placed on three-phase operation for demonstrating high power charging. Moreover, single-phase grid-tied operation with a similar topology has been demonstrated previously [36, 37]. The proposed integrated charger can also be configured as a three-phase bidirectional buck/boost converter, making DC charging possible.

The proposed integrated charger topology provides additional benefits for the electric machine itself in terms of machine life and efficiency due to the LC filter and zero sequence voltage control. Drives-related research has found that the bearings of the motor are a leading cause of failure [39, 40, 41]; moreover, the bearings are responsible for 9% of EV drive failures according to one study [42]. The causes of bearing failures are bearing voltages and currents, which are a result of the common mode voltage of injected by a switched inverter [43]. Drives research has sought to reduce bearing stresses through precision-designed passive filters [44, 45, 46], common mode voltage attenuation [47, 48] and even a type of zero sequence voltage control [49] (though not the same as is used in this paper). For best leakage current filtering, a common mode inductor is typically added irrespective of method because the zero sequence inductance of a machine is normally small unless explicitly designed for [50]. With respect to motor efficiency, the phase currents applied to the electric machine will be filtered by the added LC filter and have little PWM ripple; thus, high frequency iron loss will be reduced, with research suggesting that they can contribute significantly to total machine losses at typical drive PWM frequencies [51].

To demonstrate the proposed topology, an 11kW prototype is designed and built. To make the necessary LC filter small enough for traction applications and to increase converter efficiency, variable frequency critical soft switching is employed. Performance in traction mode is experimentally validated with torque and speed steps, as well as measurements showing that the motor leakage currents and shaft voltages are reduced by over 90% with the proposed topology. Three-phase charging mode is demonstrated with active and reactive power steps and leakage current measurements that demonstrate standard compliance for transformerless operation. Peak efficiency of the integrated charger in charging mode is measured to be 99.4% and 98.4% at rated power of 11kW. Total system efficiency in traction mode is shown to be 0.6% more efficient than standard operation when measured at 5kW output power.

II. Integrated Charger Design

A. Charger Topology Design

The proposed integrated charger, shown in Fig. 1, differs from previous research through the addition of an LC filter with the capacitor neutral point connected to the DC ground at the output of the inverter. Connection to the electric machine (traction mode) and the grid (charging mode) are both possible: in Fig. 1, this is done by using contactors to change between operating modes. Both single- [37] and three-phase [38] charging can be achieved in both configurations through control. This work focuses on three-phase operation to achieve higher power charging. The means to realize single-phase operation are shown in [37], which uses the same LC filter configuration and common mode voltage control to realize a transformerless photovoltaic inverter.

The proposed topology has several system-level benefits that make it attractive. In traction mode, the LC filter will remove the current ripple associated with typical motor drives and provide a sinusoidal voltage as opposed to a switched voltage, which will lead to an increase in drive efficiency [51] and lifetime [39, 40, 41]. In charging mode, the overall system efficiency is increased by removing the inefficient transformer [7, 52, 53, 54] due to the attenuation of the leakage current. In the subsequent sections, it is shown that the net efficiency benefit of including an LC filter with zero sequence voltage control is positive for a prototype system with no consideration of the transformer.

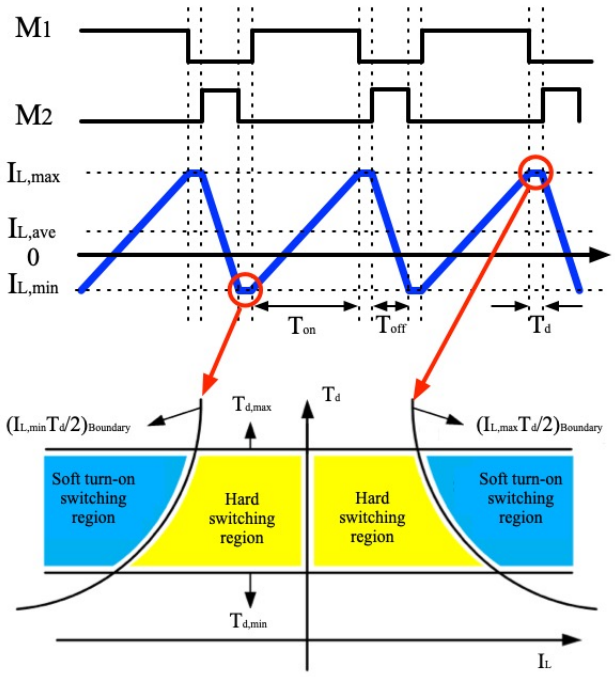

Fig. 2: Critical soft switching operating regions.

B. Critical Soft Switching

Critical soft switching technique is introduced in this section for the improvement of integrated charger efficiency [55, 56] and LC filter size reduction. The target of soft switching is to substitute the high turn-on losses of the upper switch with low turn-off losses of the lower switch in the phase legs of Fig. 1. The soft switching technique permits to increase the switching frequency by a factor of 5 and reduce the required inductance by a factor of

20. Thus, the power density can be improved with smaller size of magnetic components. Also, the switching losses are reduced with a higher efficiency. The critical soft switching method could be implemented by following the boundary conditions of dead time and peak/valley inductor current. Specifically, the product of dead time and peak/valley inductor current should be larger than a charging threshold which could be derived by the MOSFET datasheet of the switch output capacitance. Fig. 2 shows the boundary relations of upper/lower switches interlock time, T_d, and peak/valley inductor current, $I_{L,max}/I_{L,min}$, for critical soft switching operation. The blue areas are the soft switching regions which indicate enough time and current for fully discharging the switch output capacitance before turning on. The critical soft switching boundary conditions are expressed as [55, 56]

$$\tfrac{1}{2} I_{L,min} T_d \le Q_{min} \le 0, \tag{1a}$$

$$\tfrac{1}{2} I_{L,max} T_d \ge Q_{max} \ge 0, \tag{1b}$$

where Q_{min} and Q_{max} are the minimum discharging thresholds of the switch output capacitance for the soft switching. Since in the positive line cycle, a large current ripple is required to ensure negative valley inductor current to be lower than a threshold current level. In the turn-off transient period of lower switch, the negative inductor current will discharge the upper switch output capacitor. The zero voltage switching (ZVS) of upper switch can be achieved if the output capacitor is fully discharged before it turns on. Similarly, in the negative line cycle, a large current ripple is also required to guarantee the positive peak inductor current to be higher than a threshold current level. Thus, the ZVS of the lower switch can be achieved if the lower switch output capacitor is fully discharged by the positive inductor current. Thus, to achieve full soft switching in the charger operation periods, either the current ripple should be fairly large to guarantee a bidirectional inductor current paths or the dead time needs to be expanded. Since longer dead time will result in current distortion, a desired option is to adjust the switching frequency for achieving the critical soft switching in DC/AC inductor current full sinusoidal waveform range. Thus, the critical soft switching principle is implemented to maintain a constant positive threshold current in negative inductor current line cycle and negative threshold current in positive inductor current line cycle. The switching frequency can be derived with the following equation:

$$f_{sw} = \frac{(1-d) d V_{DC}}{2(|I_L| + I_{threshold}) L_f}, \tag{2}$$

where $I_{threshold}$ is the boundary threshold current for soft switching which could be derived in Fig. 2 with a given dead time and I_L is the inductor current.

C. LC Filter Design

The design of the LC filter is critical for several reasons: 1) to ensure grid standard compliance in charging mode; 2) for designing the control to avoid exciting resonances; and 3) to ensure the peak/valley inductor current ripple remains soft switching. Thus, it is beneficial to discuss its key aspects.

Because of the way the LC filter is connected, each phase looks like a buck converter with a current source load. To simplify inductor current ripple analysis, it is assumed that the capacitor voltage is approximately constant, which yields the expression

$$\Delta i_L = \frac{d\,(1-d)\,V_{DC}}{f_{sw} L_f}, \tag{3}$$

where d is the duty cycle. In a buck converter, $d = \frac{v_c}{V_{DC}}$ and the maximum ripple is reached at $d = 0.5$. To determine the inductance, a desired ripple level is specified by considering the required RMS current and peak/valley inductor current in (1) for a critical soft switching system and (3) can be solved for L_f. Inductor losses can be minimized through good design [57, 58, 59]. Since the soft switching is applied for AC inductor current to generate a large current ripple, the inductance and size of the inductor can be reduced accordingly. For the smart charger design, the switching frequency range and inductance are designed as 20-160kHz and 45μH, respectively.

With a known inductance, the filter capacitance can be found by specifying a desired voltage ripple $\Delta v_{\%}$ (e.g. 1%). It is calculated as

$$C_f = \frac{(1-d)}{8 f_{sw}^2 L_f \Delta v_{\%}}. \tag{4}$$

A potential challenge of the proposed topology is the introduction of an inductor and capacitor in the primary conduction path, which is subject to additional losses. While the filter capacitor losses can be reduced easily by paralleling several [60], the inductor remains a challenge. To reduce these losses in converters, research has been active in the design of ultra-high current inductors with high efficiency [57, 58, 59]; however, these techniques can yield bulky components. Employing variable frequency critical soft switching (VFCSS) can lead to two major benefits: 1) a net gain in converter efficiency, as was demonstrated in [55], where a 1% efficiency gain was realized even when using lossy commerical off-the-shelf inductors; and 2) a reduction in the inductance, which can lead to a smaller inductor [61]. A small inductor is strongly beneficial for on-board purposes. The extra LC filter is introduced also for the replacement of PFC function since the reactive power can be provided through control. The volume of the switch side three-phase LC filter is designed to be 11 $inch^3$ per phase. However, a typical 3.2kW single phase PFC has a volume of 24.6 $inch^3$ [62]. The added LC filter is smaller and cheaper than an extra PFC circuit, which further improves the power density.

D. Power Semiconductor

A high power density integrated charger places limitations on possible switching devices. High switching frequency is necessary to keep inductance low and, consequently, the size of the inductor small. The ability to block

high voltages and pass high current is conducive towards maximizing power capabilities. Wide-bandgap devices, such as Gallium Nitride (GaN) and Silicon Carbide (SiC) are well suited for applications such as these, and have been shown to be able to achieve similar efficiencies [63]. However, the higher blocking voltages associated with SiC devices are more applicable to the ever increasing battery voltages present in EVs. As such, the latest generation of discrete SiC devices with 1200V blocking capability were chosen for the prototype design.

III. Integrated Charger Efficiency Analysis

A. Inverter Efficiency

Losses within the switching devices and losses within magnetics are the two main sources of inefficiencies in a power converter.

1) Semiconductor Efficiency: Losses within switching devices can be approximated by calculating conduction losses and switching losses. Conduction losses for one phase can be found by

$$P_{cond} = R_{on}\left(I_{DC}^2 + \left(\frac{1}{2\sqrt{3}} I_{L,p-p}\right)^2\right) \tag{5}$$

where $\frac{1}{2\sqrt{3}} I_{L,p-p}$ is the RMS value of the peak-to-peak inductor ripple current. Switching loss calculations can be separated into two equations, one for when the converter is hard-switching and another for when the converter is soft-switching:

$$E_{sw\_hard} = E_{off}(I_{DC} - \tfrac{I_{L,p-p}}{2}, V_{ds}) + E_{on}(I_{DC} + \tfrac{I_{L,p-p}}{2}, V_{ds}) \tag{6}$$

$$E_{sw\_soft} = E_{off}(I_{DC} - \tfrac{I_{L,p-p}}{2}, V_{ds}) + E_{off}(I_{DC} + \tfrac{I_{L,p-p}}{2}, V_{ds}) \tag{7}$$

where E_{sw_hard} and E_{sw_soft} represent the FET switching loss per phase in joules per cycle as functions of I_d for constant V_{ds}. Multiplying these values by f_{sw} gives the loss in W which can be used in efficiency calculations. The turn on and turn off energies (E_{on} and E_{off} as functions of I_d for V_{ds}) are values available in the datasheet of the FET. Extrapolation for switching energies of values for V_{ds} that are not listed in the FET datasheet is done through linear interpolation of the provided values.

he entirety of the ripple current can be assumed to be absorbed in both the DC bus capacitance and the filter capacitance. This creates energy loss in the capacitances according to:

$$P_{cap} = \left(\frac{1}{2\sqrt{3}} I_{L,p-p}\right)^2 \left(ESR_{filter} + ESR_{DCbus}\right) \tag{8}$$

where the loss in each capacitance is the product of the capacitance ESR and the square of the RMS value of the inductor ripple current.

The output of this power converter is a sine wave and the values for d, I_{DC}, and $I_{L,p-p}$ are dynamic. To account for this, loss at discrete and evenly spaced points along one cycle of the sine wave is calculated by sweeping θ from 0 to 2π in

$$V_{out}(\theta) = \frac{V_{DC}}{2} + \sqrt{2} V_{out,RMS} \sin(\theta) \tag{9}$$

$$I_{DC}(\theta) = \sqrt{2} I_{out,RMS} \sin(\theta - \phi) \tag{10}$$

$$I_{L\_ripple\_p-p}(\theta) = \frac{d(1-d)V_{DC}}{L_f \cdot f_{sw}} \tag{11}$$

$$d(\theta) = \frac{V_{out}(\theta)}{V_{DC}}. \tag{12}$$

to provide d, I_{DC}, and $I_{L,p-p}$ which are used in conjunction with (5) and (6) to calculate the loss at these discrete points. The loss at each discrete point is then averaged together to obtain the average loss over one cycle of the sine wave.

2) Inductor Efficiency: The losses in the LC magnetics of the inverter are the other main source of inefficiency. Especially for the switching side inductor, most of the current ripples are handled by this part of the magnetics. A precise estimation of LC inductor losses as a function of switching frequency could contribute to understanding the optimal operating frequency. The inductor losses are mainly composed of core losses and copper losses. For the core selection, E42/21/20-3F3 from Ferroxcube is used for a compact design of the inductor. Due to the high permeability of the chosen material, air-gap is introduced for adjusting the inductance to the desired value of $45\mu H$. The core losses of the air-gapped inductor are derived from

$$P_{core} = k f_{sw}^a B_{pk}^b = k f_{sw}^a \left(\frac{4\pi N I_{pk} 10^{-2}}{l_g + (l_m/\mu_r)}\right)^b \tag{13}$$

where k, a, b are the coefficients for the core material, B_{pk} is the peak flux density, f_{sw} is the switching frequency, $N, I_{pk}, l_g, l_m, \mu_r$ are the turn number, peak current, air-gap, and length of the magnetic path and permeability, respectively.

For the copper losses, AC and DC losses are the two main sources. To further improve the efficiency of inductor in high frequency application, litz wire of equivalent AWG10 is applied for the winding. Thus, the AC losses caused by the skin and proximity effects could be significantly reduced. The copper losses with litz wire are expressed as

$$P_{Cu} = I_{fund,RMS}^2 R_{fund} + I_{PWM,RMS}^2 R_{PWM} \tag{14}$$

where $I_{fund,RMS}, I_{PWM,RMS}$ are the RMS current of motor fundamental and PWM carrier frequency components. This allows for the inductor losses to be calculated under the same operating point as the previously derived semiconductor losses. Litz wire is used for the windings of the inductors of this converter and the high frequency AC losses caused by R_{PWM} can be reduced. For the reason to apply a custom designed inductor instead of commercial off-the-shelf one, the temperature rise is taken into the most consideration. Most of the commercial high current inductors leverage the solid magnetic winding which can generate significant copper losses at high frequency due to a high AC resistance factor and the temperature rise can reach above 100°C. Also, for the application of soft switching, a large current ripple can produce high core losses as is

shown in 13 which needs careful attention to design the airgap.

Projected inverter efficiency calculations using this method at 8kW, 835V DC bus, $400V_{LL}$, and utilizing VFCSS is 98.9% which matches with the experimental inverter efficiency results seen in Fig. 18.

B. Motor Efficiency

Motor losses consist of three main components: winding losses $P_{PMSM,winding}$, core losses $P_{PMSM,core}$, and mechanical losses $P_{PMSM,mech}$. Rigorously quantifying motor loss is a complex exercise that typically requires finite-element analysis for most accurate results [64]. However, it is possible to measure motor loss components experimentally and disaggregate motor loss components. Specifically, it is possible to measure total motor losses $P_{PMSM,total}$; measure the AC winding resistance at fundamental and PWM frequency and quantify the winding losses $P_{PMSM,winding}$; and measure the baseline machine losses $P_{PMSM,baseline}$, i.e. the losses of a rotating PMSM with inverter off that consist of the mechanical (bearing and windage) losses and the core losses due to the PM field (without phase currents, i.e. additional core losses due to the armature reaction created by the phase currents).

From the above loss components, it is possible to calculate the remaining core losses due to the armature reaction

$$P_{PMSM,coreA} = P_{PMSM,total} - P_{PMSM,winding} - P_{PMSM,baseline} \quad (15)$$

where P_{total} is measured total system loss. The inverter loses are measured experimentally and split into FET, inductor, and capacitance losses in conjunction with the methods shown in the previous section. The PMSM baseline loss is measured and consists of the mechanical loss and the core loss due to PM flux when the inverter is disconnected. PMSM winding loss calculated in conjunction with the measured frequency dependant winding resistance. The PMSM core loss is then calculated as the difference between the total measured loss and all other loss mechanisms present in the converter.

C. Net Impact

Fig. 3 shows the loss breakdown for a Marathon Motors 213TPFSA10096 running at 1200RPM and 700V DC bus with inverter configurations of f_{sw} = 20kHz without an LC filter, f_{sw} = 80kHz without an LC filter, f_{sw} = 80kHz with an LC filter, and variable frequency critical soft switching with a range of $20kHz < f_{sw} < 160kHz$ with an LC filter. 20kHz switching frequency was chosen for the configuration without the LC filter as this is a common value for typical motor inverters. 80kHz switching frequency was chosen for operation with the LC filter as this value yields a suitable inductor ripple current without incurring extra switching losses by unnecessarily driving up switching frequency.

It can be in Fig. 3 seen that the proposed integrated charger topology reduces the total losses when compared to a typical motor inverters without an LC filter. The additional losses incurred by the LC filter are negated through a larger decrease in PMSM core loss. Furthermore, the variable frequency critical soft switching allows for an increase in switching frequency without increasing the PMSM core loss which can be used to minimize the size of this additional LC filter.

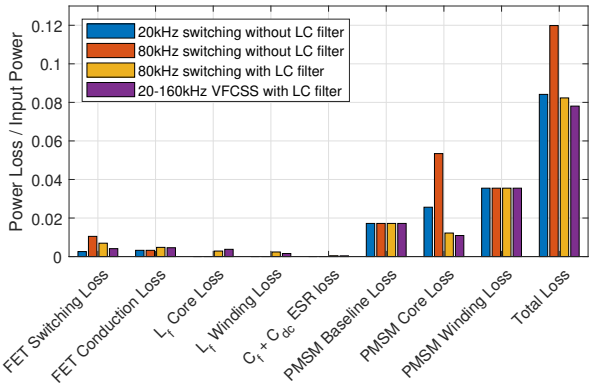

Fig. 3: PMSM drive system power loss components for each converter configuration at 5kW input power.

IV. System Modelling and Control

A. System Modelling

To simplify development of the model, the LC filter subsystem is first studied. The differential equations governing the LC filter are

$$\dot{i}_{L,abc} = \frac{1}{L_f} v_{x,abc} - \frac{1}{L_f} v_{c,abc} \quad (16a)$$

$$\dot{v}_{c,abc} = \frac{1}{C_f} i_{L,abc} - \frac{1}{C_f} i_{o,abc} \quad (16b)$$

where $v_{x,abc}$ and $v_{c,abc}$ are the inverter and capacitor three-phase voltages and $i_{L,abc}$ and $i_{o,abc}$ are the three-phase inductor and output currents.

It can be difficult to track sinusoidal values with typical control schemes like proportional-integral (PI) controllers. Hence, it is beneficial to apply the Clarke and Park transforms to convert the system to equivalent DC quantities. The transforms are applied as $x_{dq0} = \mathbf{P}(\theta)\mathbf{T}x_{abc}$, where the variable x represents either voltage or current. The magnitude invariant Clarke transform is

$$\mathbf{T} = \frac{2}{3}\begin{bmatrix} 1 & -\frac{1}{2} & -\frac{1}{2} \\ 0 & \frac{\sqrt{3}}{2} & -\frac{\sqrt{3}}{2} \\ \frac{1}{2} & \frac{1}{2} & \frac{1}{2} \end{bmatrix}. \quad (17)$$

and the Park transform is

$$\mathbf{P}(\theta) = \begin{bmatrix} \cos\theta & \sin\theta & 0 \\ -\sin\theta & \cos\theta & 0 \\ 0 & 0 & 1 \end{bmatrix}. \quad (18)$$

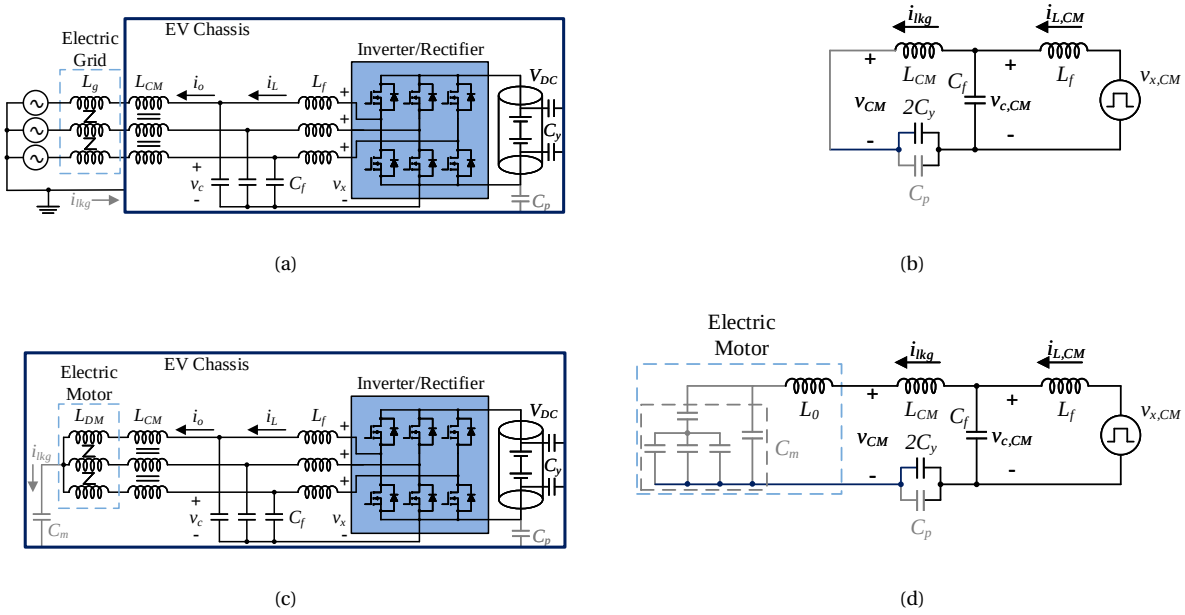

Fig. 4: Circuit diagrams of the proposed integrated charger. (a) Charging mode. (b) Equivalent common mode of charging mode. (c) Traction mode. (d) Equivalent common mode of traction mode.

Applying the Clarke and Park transforms to (16) yields the $dq0$ equations of the LC filter

$$\dot{i}_{L,dq0} = \frac{1}{L_f} v_{x,dq0} - \frac{1}{L_f} v_{c,dq0} - \omega \mathbf{J}_{LC} i_{L,dq0} \tag{19a}$$

$$\dot{v}_{c,dq0} = \frac{1}{C_f} i_{L,dq0} - \frac{1}{C_f} i_{o,dq0} - \omega \mathbf{J}_{LC} v_{c,dq0} \tag{19b}$$

where ω represents the angular velocity of the sinusoidal AC signal and $\mathbf{J}_{LC}$ is the cross-coupling matrix of the LC filter, which is written as

$$\mathbf{J}_{LC} = \begin{bmatrix} 0 & -1 & 0 \\ 1 & 0 & 0 \\ 0 & 0 & 0 \end{bmatrix}.$$

With the LC filter subsystem developed, the output, i.e. the three-phase grid or traction motor, can be added to complete the integrated charger model. In both traction and charging modes, it can be assumed that the neutral point is isolated, meaning that the zero sequence component can be ignored. In charging mode, the three-phase grid is modelled as voltage sources at the point of common connection at the capacitors. In traction mode, the motor terminal voltages, normally referred to as v_{dq} in drives literature, are now $v_{c,dq}$; likewise, the motor currents, normally referred to as i_{dq}, are now $i_{o,dq}$ in the topology. Changing the notation of the standard PMSM model yields

$$\dot{i}_{o,d} = \frac{1}{L_d}\left(v_{c,d} - R_s i_{o,d} + \omega L_q i_{o,q}\right) \tag{20a}$$

$$\dot{i}_{o,q} = \frac{1}{L_q}\left(v_{c,q} - R_s i_{o,q} - \omega\left(L_d i_{o,d} + \psi\right)\right) \tag{20b}$$

where L_d and L_q are the d- and q-axis inductances of the motor, respectively; R_s is the stator winding resistance; ψ is the flux of the permanent magnets; and ω is the electrical angular velocity of the rotor, which is linked to the mechanical angular velocity ω_m by the pole pairs p_p by $\omega = p_p \omega_m$.

B. Common Mode Modelling

The leakage current in a system with a parasitic capacitance C_{lkg} between the DC negative and AC neutral can be written as

$$i_{lkg} = C_{lkg} \frac{dv_{CM}}{dt} \tag{21}$$

where v_{CM} is the common mode voltage resulting from the switching operations. This voltage changes rapidly in a switched circuit as a high switching frequency is advantageous for reducing the size of passive components (inductors and capacitors). It is calculated as

$$v_{CM} = \frac{1}{3}\left(v_{x,a} + v_{x,b} + v_{x,c}\right), \tag{22}$$

where v_x is the voltage at the output of the inverter. In a typical inverter, $v_x \in \{-\frac{1}{2}V_{DC}, +\frac{1}{2}V_{DC}\}$; in the proposed topology, $v_x \in \{0, +V_{DC}\}$.

To study the system and to determine the impact of the proposed topology with LC filter on the common mode, the parasitic couplings can be added to Fig. 1, resulting in Fig. 4. Using Fig. 4a and Fig. 4c, the common mode equivalent circuits Fig. 4b and Fig. 4d can be determined, which both have a parasitic capacitance C_p coupling chassis to the DC negative and a battery common mode noise filtering *Y capacitance* C_y present. In traction mode (Fig. 4d) the equivalent motor common mode circuit of Fig. 5 is included that has a zero sequence inductance L_0, which is normally small [50], and the parasitic capacitances of the motor that

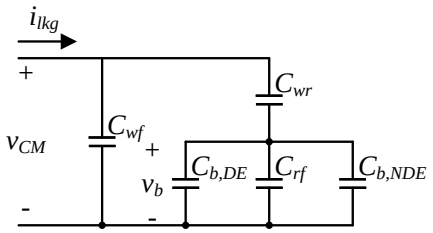

Fig. 5: Equivalent electric machine common mode circuit.

couple to chassis called C_m, whereas in charging mode there is no capacitance beyond C_p and C_y. The parasitic capacitances in each individual mode can be summed together to yield the total leakage capacitance C_{lkg}, which is what interacts with the common mode voltage to generate the leakage current i_{lkg}. In traction mode, owing to the higher impedances afforded by L_0 and C_m, the leakage current should be smaller than in charging mode.

In a typical inverter, a common mode inductor L_{CM} is used to attenuate the leakage current i_{lkg}, though it is not sufficient by itself. In the proposed integrated charger topology, a common mode inductor is also used to further attenuate the leakage current beyond what is already achieved with the common mode voltage control to ensure charging mode leakage current standard compliance.

1) Motor Bearings: Bearing currents and voltages are a major point of failure for electric drives [42]. Modelling their frequency and magnitude is difficult [65]; however, the literature is clear: they are generated by the common mode voltage v_{CM} [43].

A widely cited simplified equivalent circuit of the electric machine's parasitic capacitances can be considered, shown in Fig. 5 [39, 40, 41], to help with understanding the benefit the proposed integrated charger topology has for the motor bearings. A useful ratio called the *bearing voltage ratio* can be calculated from it that is indicative of the bearing voltage in the system. It is

$$BVR = \frac{C_{wr}}{C_{wr} + C_{b,NDE} + C_{rf} + C_{b,DE}}, \tag{23}$$

where $C_{b,NDE}$ and $C_{b,DE}$ are the non-drive end and drive end parasitic capacitances of the bearings, respectively, C_{wr} is the stator winding to rotor capacitance and C_{rf} is the rotor to frame capacitance. Typical BVRs are less than 10% [66] but vary depending on the specific motor [67]. The bearing voltage can then be calculated as

$$v_b = v_{CM} BVR. \tag{24}$$

The common mode voltage seen at the motor's terminals with the proposed integrated charger can be broken into two components: a fixed (DC) value across the capacitor $v_{c,CM}$ and an AC disturbance signal v_{AC} superimposed that represents ripple in the control, noise, etc. This gives the common mode voltage

$$v_{CM} = v_{c,CM} + v_{AC}. \tag{25}$$

With a well designed control, v_{AC} will be small, which means that the bearing voltage will be $v_b = \left(v_{c,CM} + v_{AC}\right) BVR$, i.e. a small DC offset and a very small disturbance due to the switching and control. By keeping $v_{c,CM}$ below the breakdown voltage of the lubricant, damaging electric discharge machining bearing currents can be avoided with the proposed topology.

An approximation of the bearing currents can be obtained by recognizing that the leakage current i_{lkg} will be divided between C_{wf} and the bearing path. According to the literature, C_{wf} has a low impedance compared to the bearing path [46]; hence, the bearing current i_b will be a fraction of the leakage current. With the proposed topology, v_{CM} is kept approximately constant, which means that i_{lkg} will be small and, thus, i_b will be very small.

C. Control

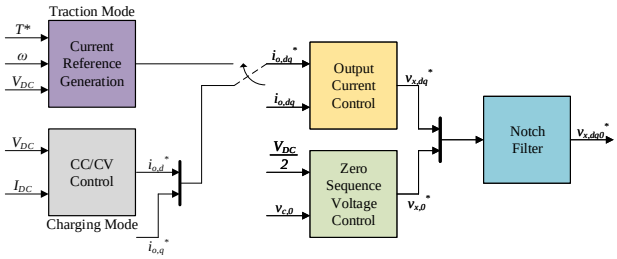

Fig. 6: Proposed integrated charger control block diagram.

Control is realized in the $dq0$ frame. Transfer functions can be derived for the d- and q-axes by solving the differential equations (19) and (20) for the desired input-output relationship. To simplify the implementation, the inductor currents are not directly controlled and, instead, the output current is used to generate the reference voltage for the inverter to apply, meaning that the transfer functions $H_d(s) = \frac{i_{o,d}}{v_{x,d}}$ and $H_q(s) = \frac{i_{o,q}}{v_{x,q}}$ are solved for. A benefit of this strategy is that the inductor current sensors can be omitted, reducing added costs.

Like in the dq axes, the 0-axis transfer function can be derived from the differential equations (19). For the control design, the equivalent leakage capacitance C_{lkg} and the common mode inductance L_{CM} are omitted. This is because C_{lkg} is small and, hence, has a high impedance; the common mode inductance also has a high impedance. Simplifying in this way helps to build the transfer function that links the capacitor voltage with the inverter input voltage, which is given by

$$H_{CM}(s) = \frac{v_{c,CM}}{i_{L,CM}} \times \frac{i_{L,CM}}{v_{x,CM}} = \frac{v_{c,CM}}{v_{x,CM}}. \tag{26}$$

This transfer function makes clear that the capacitor's common mode voltage is controllable. To maximize voltage utilization, $v_{c,CM}$ should be controlled to $\frac{1}{2}V_{DC}$.

Care must be taken when designing the control of this system because of the small LC filter parameters, as resonance will be exhibited in all three axes at

$$\omega_{res,d} = \sqrt{\frac{L_{o,d}+L_f}{L_{o,d}L_fC_f}} \tag{27a}$$

$$\omega_{res,q} = \sqrt{\frac{L_{o,q}+L_f}{L_{o,q}L_fC_f}} \tag{27b}$$

$$\omega_{res,0} = \sqrt{\frac{1}{L_fC_f}} \tag{27c}$$

where L_o is the output inductance of the system. In traction mode, the output inductances are the motor inductances, i.e. $L_{o,d} = L_d$ and $L_{o,q} = L_q$; in charging mode, the output inductance is the intrinsic inductance of the grid, i.e. $L_{o,d} = L_{o,q} = L_g$.

To compensate for the resonance, a notch filter can be added at the cutoff frequency of each of the $dq0$-axes. The notch filter can be designed in continuous-time as

$$\frac{s^2+\omega_{res}^2}{s^2+\frac{\omega_{res}}{Q}+\omega_{res}^2} \tag{28}$$

and implemented in discrete-time as difference equations. The variable Q represents the quality factor of the filter and can be used to tune how wide the notch is. The Bode plots of the system with and without notch filters are shown in Fig. 7, with the resonance clearly being attenuated when applied. The phase and gain margins of each axis with notch filter indicate the proposed control scheme is stable at 20kHz control frequency, whereas without it is not.

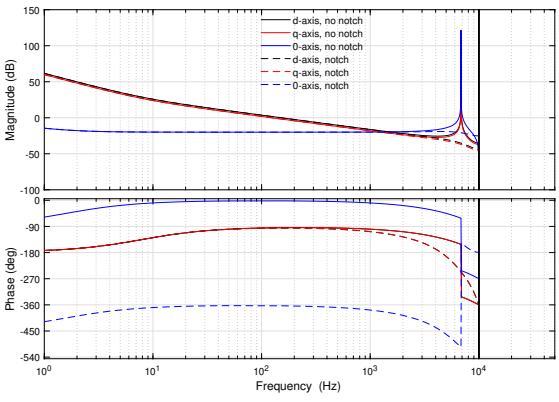

Fig. 7: Bode plots of the proposed control scheme with (dashed lines) and without (solid lines) notch filter.

The proposed control structure is shown in Fig. 6, where traction and charging modes share the same fundamental output current and zero sequence voltage control, but differ in how the reference output currents $i^*_{o,dq}$ are generated. In traction mode, the reference currents can be obtained from some reference generation scheme, e.g. maximum torque per Ampère. In charging mode, a constant current/constant voltage (CC/CV) controller is employed, which demands a d-axis current reference $i^*_{o,d}$ to deliver active power and, if grid support is necessary, a reactive power reference $i^*_{o,q}$ can be added as well. The CC/CV controller has two states: the first pushes a constant current until the battery's state-of-charge (SOC) is near peak; the second applies a constant voltage that trickle charges to complete the charging cycle [68].

D. Phase-Locked Loop

To obtain the grid's phase in charging mode, a phase-locked loop (PLL) is employed. Its design follows a standard synchronous reference frame (dq) implementation, such as the one described in [69], where the grid voltages at the point of common connection with the grid (the capacitors) are measured. The common mode voltage control does not influence the design of the PLL as it infers the grid's phase θ from the $\alpha\beta$ voltages, which have the zero sequence component separated from them through the Clarke transform.

V. Experimental Results

The proposed integrated charger topology is experimentally validated in both traction and charging modes with the parameters provided in Table II. The prototype integrated charger is designed for EVs with minimum, nominal and maximum battery voltages of 700V, 835V and 900V, respectively. Traction mode is demonstrated with torque and speed steps to show that dynamic performance is not degraded compared to a standard drive and that a reduction in leakage currents and shaft voltages are seen. Charging mode test conditions emulate interfacing with the 50Hz European three-phase grid with line voltage 400V$_{LL}$ and show active and reactive power steps as well as leakage current compliance. The prototype has rated power of 11kW with RMS phase current of 16A at V_{LL} = 400V. The experimental setups are depicted in Fig. 8, with Fig. 8a showing traction mode and Fig. 8b charging mode.

TABLE II: Prototype integrated charger system parameters.

Parameter	Value
PMSM pole pairs (p_p)	5
PMSM stator resistance (R_s)	0.4Ω
PMSM d-axis inductance (L_d)	10.5mH
PMSM q-axis inductance (L_q)	12.9mH
Permanent magnet flux (ψ)	0.3491Wb
Filter inductance (L_f)	45μH
Filter capacitance (C_f)	12μF
Common mode inductance (L_{CM})	4mH
Minimum DC voltage	700V
Nominal DC voltage	835V
Maximum DC voltage	900V
Rated power	11kW

A. Traction Mode

Traction mode validation is demonstrated with torque and speed steps and steady state operation with DC voltage

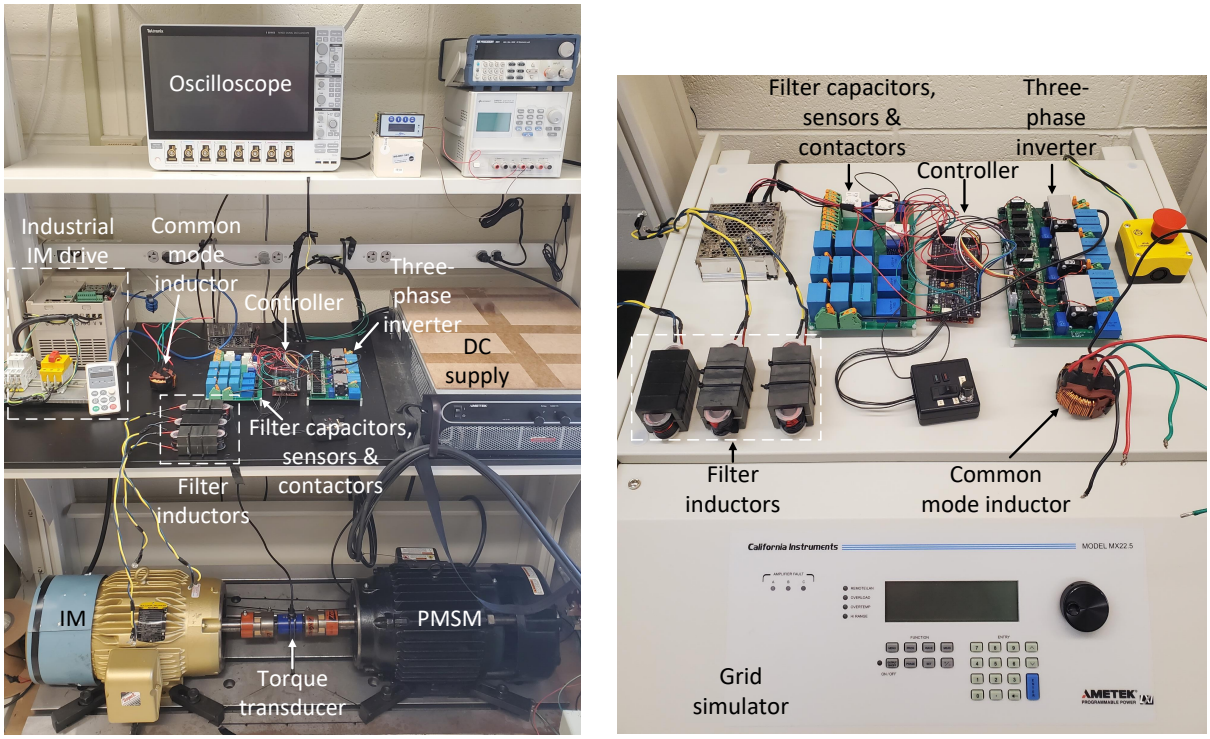

(a) (b)

Fig. 8: Experimental setups of the proposed integrated charger. (a) Traction mode. (b) Charging mode.

V_{DC} = 700V. The goal is to show that the steps and subsequent steady state operation are similar to a standard drive, i.e. without LC filter and zero sequence voltage control. In this setup, shown in Fig. 8a, an IM and PMSM are coupled together with the IM connected to an off-the-shelf variable frequency drive (VFD) and the PMSM connected to the proposed integrated charger.

Torque control validation is shown through a sequence of torque steps from zero torque to maximum torque in both motor (positive torque) and generator (negative torque) operation before resting at the final commanded torque ($i_{o,q}$ = +5A) at speed N = 1000RPM, with the results shown in Fig. 9. In torque control mode, the induction machine's speed is set by the VFD and the PMSM is used to generate torque. Both the dynamic and steady state performance are not degraded relative to the same testing configuration without LC filter and zero sequence voltage control [4]. The practical bandwidth of the control is approximately 200Hz, found by calculating $\frac{0.35}{t_{rise}}$ [70], which is consistent with the Bode plots of Fig. 7.

Speed control emulates how a vehicle responds to the driver pressing down on the pedal to accelerate. In this test case, the IM is disconnected from the VFD and the PMSM's speed is controlled. To demonstrate speed control performance, positive (acceleration) and negative (deceleration) speed steps are applied, which are shown in Fig. 10. The dynamic performance is not degraded relative to the same motor drive without LC filter and zero sequence voltage control [5]. Together with the torque control results, the proposed integrated charger topology is shown to be feasible in traction mode.

An additional benefit conferred by the proposed integrated charger topology is a reduction in bearing currents and shaft voltages. As discussed in section IV-B, these phenomena are directly linked to the common mode voltage. Because the proposed topology controls v_{CM} to an approximately constant value, a reduction in v_b and i_{lkg} can be seen. The reduction in v_b is shown by measuring the shaft voltage v_{shaft} of the machine and i_{lkg} is shown by measuring the leakage current at the motor's terminals. Four cases are measured with the same switching frequency f_{sw} = 80kHz so as to make a direct comparison: 1) no LC filter (and, hence, no common mode voltage control) and no common mode inductor to demonstrate baseline leakage current of the drive, shown in Fig. 11a; 2) no LC filter with common mode inductor; 3) LC filter with no common mode inductor, to demonstrate the benefit the common mode voltage control provides by itself; 4) LC filter with common mode inductor to show the additional bearing voltage and leakage current attenuation provided by augmenting the common mode current path, shown in Fig. 11b. Results are summarized in Table III. The proposed control reduces the peak-to-peak leakage current by 94% and the RMS leakage current by 97% and the peak-to-peak shaft voltage by 90%. The common mode voltage is controlled well, with a small sinusoidal oscillation and peaks injected by the switching actions. The peaks can be reduced by slowing switching transients down by using

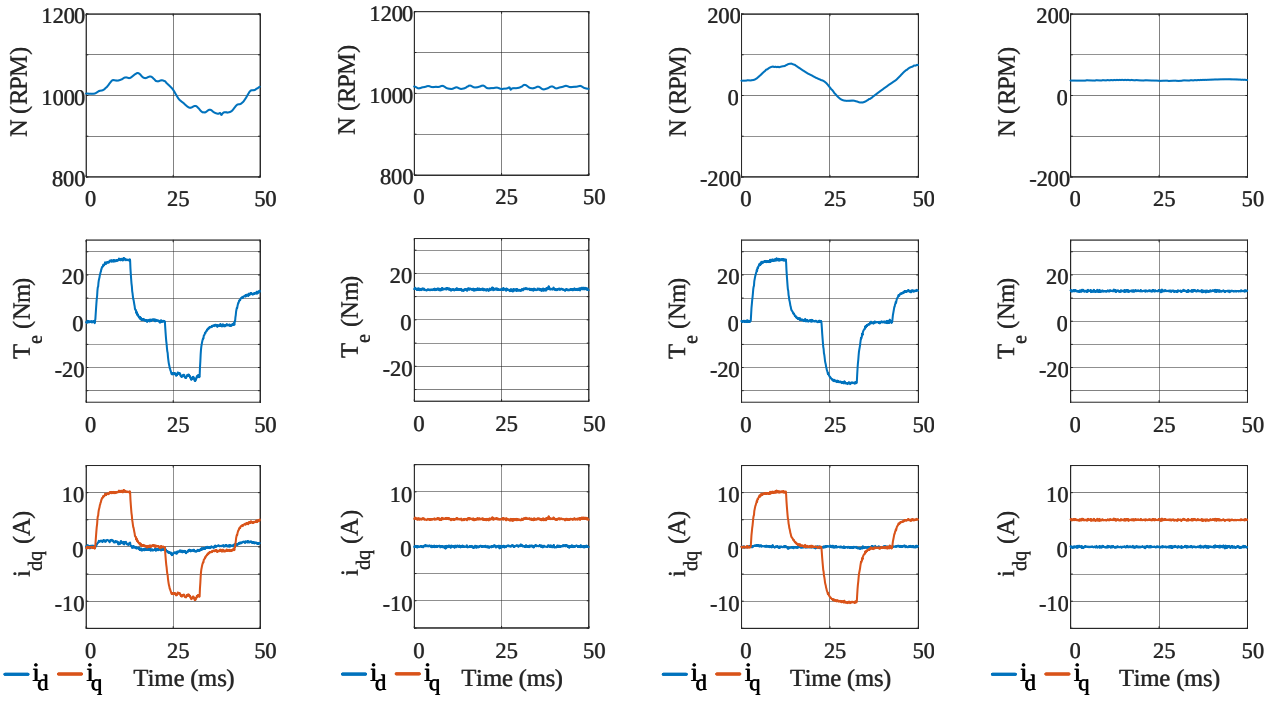

Fig. 9: Traction mode experimental torque control validation with $i_{o,d} = 0$A at high ($N = 1000$RPM) and low ($N \approx 30$RPM) speed. (a) High speed torque step sequence. (b) High speed steady state torque. (c) Low speed torque step sequence. (d) Low speed steady state torque.

Silicon MOSFETs or IGBTs or by adding gate resistance or a snubber; however, all of these options will reduce inverter efficiency.

TABLE III: Leakage current measurements of the PMSM drive with and without LC filter and common mode inductance at $N = 600$RPM.

Test Condition	Peak-to-Peak	RMS
No LC filter, $L_{CM} = 0mH$	4.92A	458mA
No LC filter, $L_{CM} = 4mH$	1.68A	393.5mA
LC filter, $L_{CM} = 0mH$	0.578A	34.23mA
LC filter, $L_{CM} = 4mH$	0.272A	15.78mA

The filtering of the currents and voltages applied to the traction machine will lead to an increase in efficiency. This is demonstrated experimentally by measuring the output mechanical power of the system $P_m = T_L\omega_m$ and dividing it by the input power to the system $P_{in} = V_{DC}I_{DC}$ at $N = 1200$RPM in four cases: 20kHz switching with no LC filter, which represents a standard traction drive; 80kHz with no LC filter, which is a standard drive topology at a higher switching frequency; 80kHz with the proposed toplogy, which does not always achieve soft switching; and the variable frequency critical soft switching implementation of the proposed topology. The results of the efficiency measurements are presented in Fig. 12, where it can be seen that the variable frequency drive has the highest efficiency and is 0.6% more efficient at maximum power than the 20kHz standard drive. The PMSM's peak efficiency is 93%, per its datasheet.

B. Charging Mode

Three-phase charging mode validation is demonstrated with steady state energy conversion modes, transients of active and reactive power steps and leakage current with RMS value lower than 30mA. 6kW steady state inductor current, grid voltage, battery current and battery voltage waveforms are shown in Fig. 13 at battery voltage of 835V and grid voltage of 400V_{LL}. It can be seen that the peak inductor current is always greater than zero and the valley inductor current is always less than zero, which means that critical soft switching is maintained over a full line cycle. The relationship between the variable switching frequency and the measured inductor current is shown in Fig. 14, where the switching frequency varies from 50-160kHz over the line cycle. A higher current will require a lower switching frequency to achieve soft switching, with 20kHz the lower limit permissible in the prototype system.

And the power step of 5kW is performed in Fig. 15 with the transient waveforms. Based on the capabilities of controlling active/reactive power, the charger can compensate for the fluctuation of grid frequency/grid voltage with desired active/reactive power. Different reactive power demands are plotted in Fig. 16 to verify the reactive power

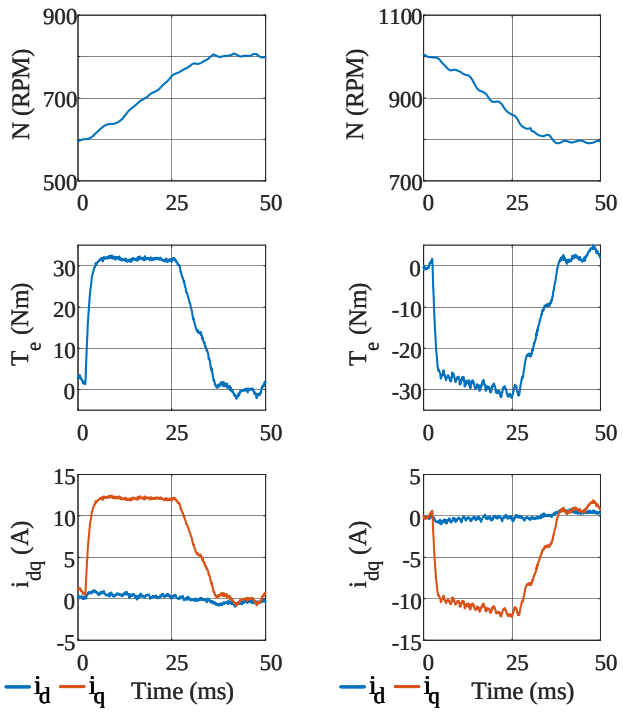

Fig. 10: Traction mode experimental speed validation with $i_{o,d} = 0$A. (a) Acceleration ($N = 600$RPM $\rightarrow$ $N = 800$RPM). (b) Deceleration ($N = 1000$RPM $\rightarrow$ $N = 800$RPM).

capability. Thus, the charger can provide grid services in compliance with IEEE1547, such as the grid voltage-reactive power mode and frequency-active power mode. Specifically, when the grid voltage/frequency are detected lower than rated value, the charger can increase the reactive/active power to be generated. Otherwise, the charger can reduce the generated reactive/active power.

To demonstrate the attenuation of the leakage current through the proposed topology, the leakage current waveforms are shown in Fig. 17. The LC filtered topology is tested in two cases: (1) with a 4mH common mode choke; (2) without common mode choke. The RMS leakage current are both below 30mA, which is comparable to a single-phase non-isolated photovoltaic inverter operating at lower AC and DC voltages [37] and satisfies standards permitting transformerless operation [31, 32, 33]. Like in traction mode, the common mode voltage is well controlled, albeit with spikes during switching transients. These can be reduced by slowing the switching transients, but this would come at the expense of system efficiency. Given the leakage current compliance, the configuration is deemed acceptable.

The efficiency of the proposed integrated charger under different load and line conditions was measured to demonstrate its viability. Results are shown in Fig. 18, where the nominal DC voltage of 835V was applied with ±10% variation in the nominal AC line-to-line voltage of 400V. Peak efficiency is 99.4% and minimum efficiency at rated

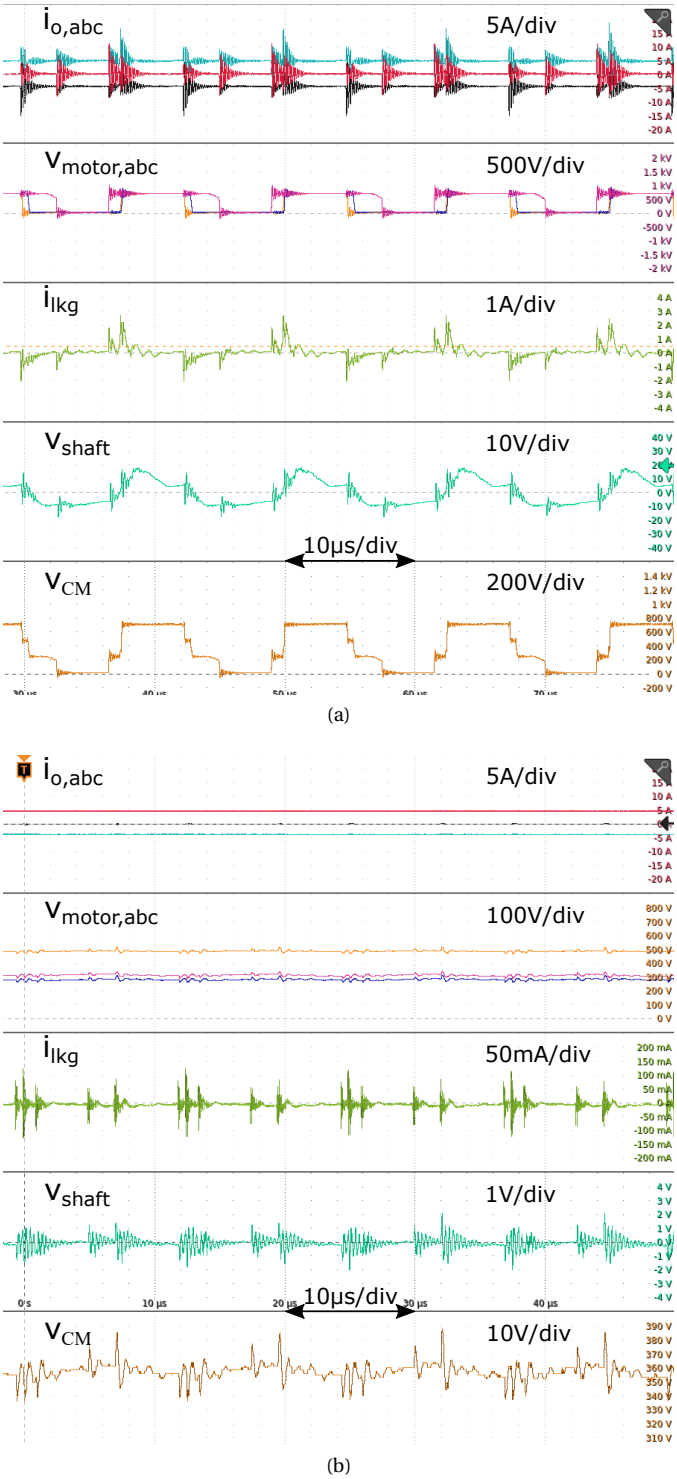

Fig. 11: Leakage current and shaft voltage waveforms of a standard inverter and proposed topology with $f_{sw} = 80$kHz. (a) Standard topology. (b) Proposed topology.

power is 98.4%. Other results in literature are in the range of 93-95% for 3.3kW add-on interface integrated chargers with 400V batteries [26, 27, 28], 90-95% for 6.6kW integrated chargers with six-phase machines [71] and 80% for a split-phase three-phase PMSM operating at 2kW [10]. Non-integrated on-board chargers, i.e. units dedicated solely to

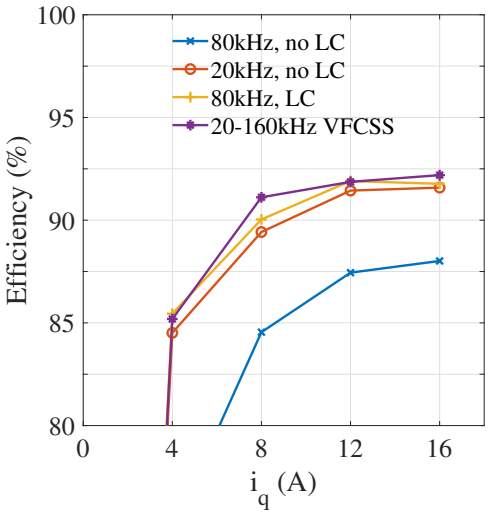

Fig. 12: Measured total system efficiencies in traction mode at N = 1200RPM with different configurations. Peak efficiency of the PMSM is 93%, per its datasheet.

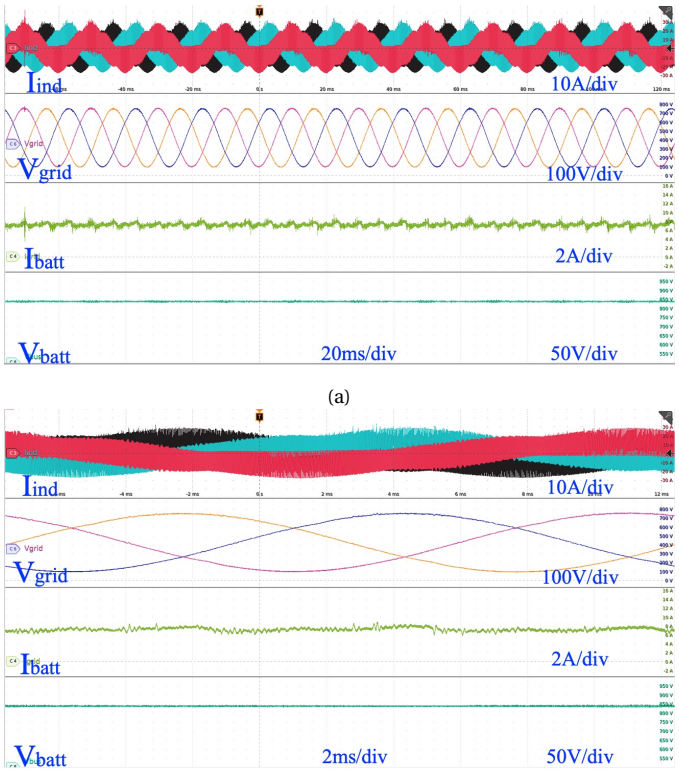

Fig. 13: Steady state charging mode waveforms of (a) inductor current, grid voltage, battery current and battery voltage and (b) zoomed out waveforms at 6kW.

charging, have been shown to be up to 97% efficient at 22kW, though they require substantial numbers of components, and commercially available on-board chargers are up to 95% efficient [12]. Therefore, the proposed topology performs well while providing net efficiency and reliability

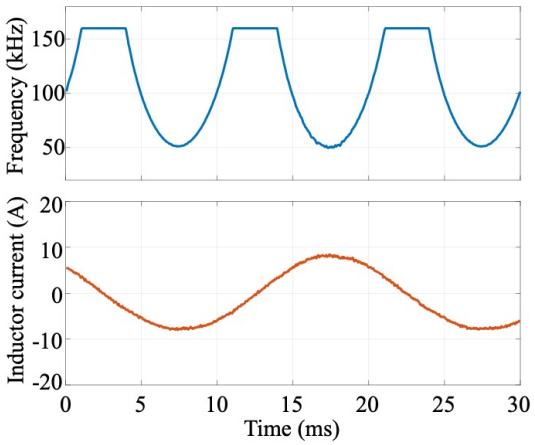

Fig. 14: The switching frequency is adjusted to force soft switching based on the measured (average-sampled) inductor current.

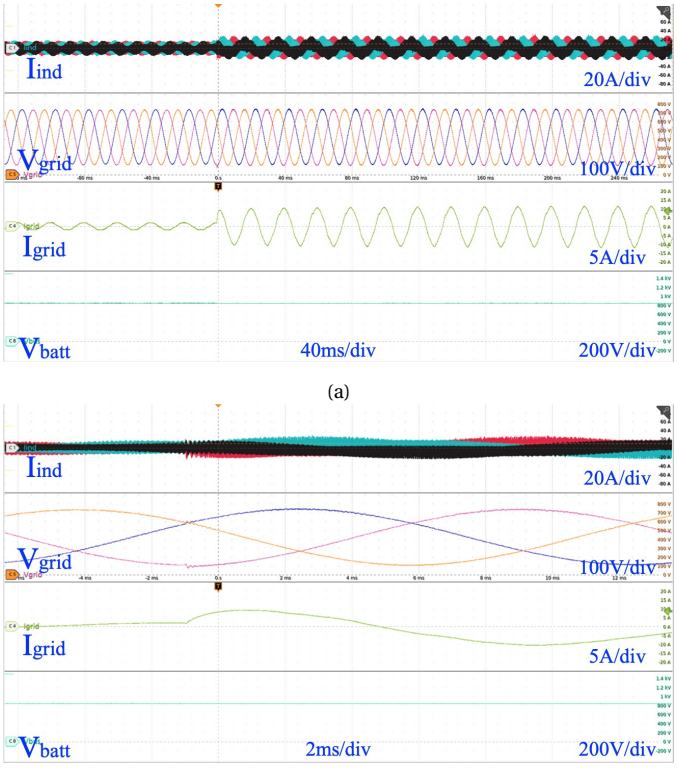

Fig. 15: Inductor current, grid voltage, grid current and battery voltage waveforms with (a) active power step of 5kW (b) zoomed waveforms during transient.

benefits in traction mode and removing the need for an isolation transformer in charging mode.

VI. Comparison of Proposed Integrated Charger to United States Department of Energy Targets

The proposed integrated charger concept removes the dedicated on-board charger and replaces it with several necessary components that are non-standard for an electric

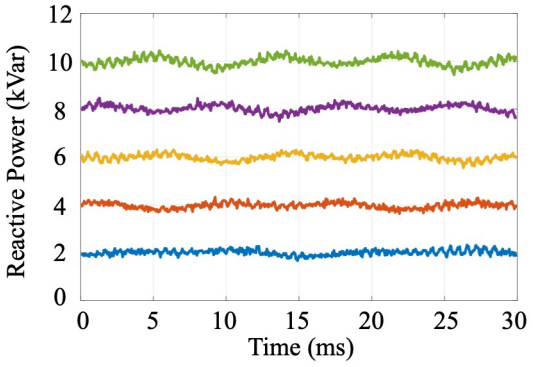

Fig. 16: Reactive power commands from 2kVAR to 10kVAR with a step of 2kVAR captured in a time range of 30ms.

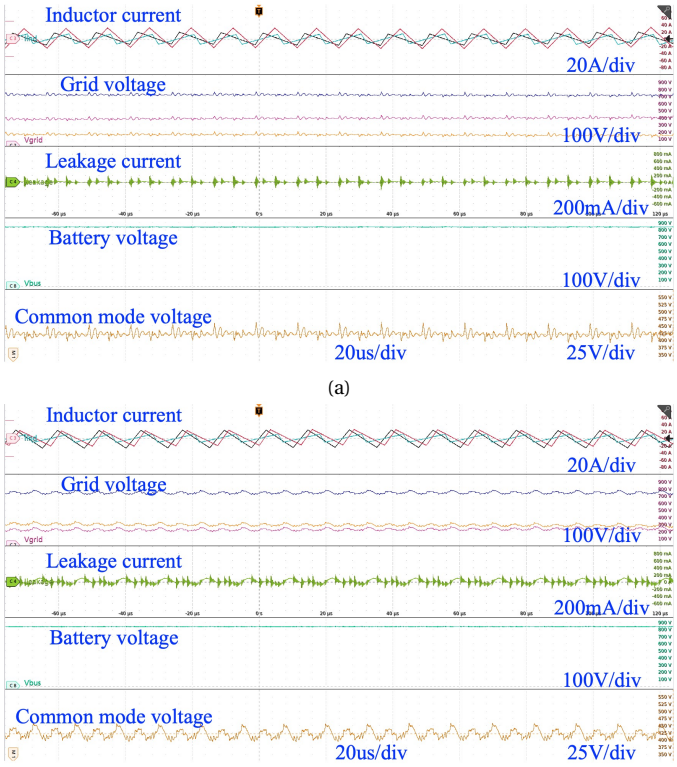

Fig. 17: Inductor current, grid voltage, leakage current, battery voltage, common mode voltage (a) with common mode choke in the loop and (b) without common mode choke in the loop.

vehicle drive. The unit cost, weight, volume and quantity of the added components are listed in Table IV. The total cost of a single prototype is $280.16, which could be reduced significantly when moving to mass production and is significantly lower than the US DOE targets for a mass produced dedicated on-board charger unit. The added mass and required volume are also fairly low, with a large portion of both dedicated to the filter inductors.

When comparing to the US DOE targets outlined in Table I, the single prototype of the integrated charger performs very well in all metrics for the 2020 targets and for most

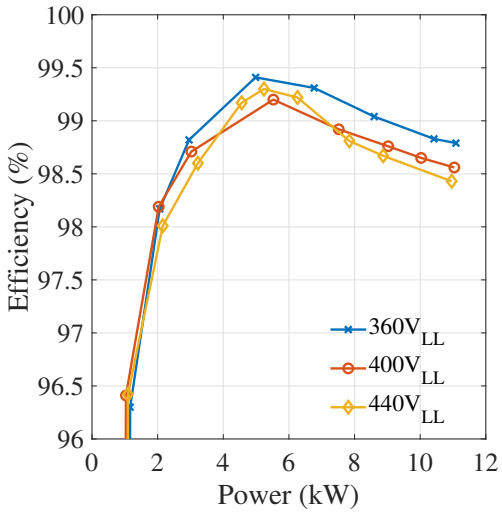

Fig. 18: Measured efficiency of the variable frequency critical soft switching integrated charger in charging mode.

TABLE IV: Unit cost, weight, size, and quantity of the components necessary for one prototype unit of the proposed integrated charger.

Component	Cost ($)	Mass (kg)	Volume (L)	Quantity
Filter inductor	50	0.9	0.182	3
Filter capacitor	6	0.029	0.026	3
CM inductor	13.48	0.215	0.159	1
Voltage sensor	9	0.01	0.0005	3
Contactor	6.28	0.017	0.01	3
RCD	34	0.36	0.182	1
TOTAL	280.16	3.44	1.22	-

in the 2025 ones. This is outlined in Table V, where the US DOE targets are for mass production of 500,000 units and the prototype metrics are evaluated for a single unit with low volume pricing. Relative to the US DOE targets in 2020 and 2025, the single prototype is 49.1% and 27.2% cheaper, respectively, with the gap expected to grow if the prototype were optimized for cost and brought to mass production. The specific power is marginally higher compared to the 2020 target but below the 2025 target, where significant gains can be made through shrinking of the filter inductors. The power density is almost three times higher than the 2020 target and almost two times the 2025 target. Lastly, the peak efficiency of the integrated charger is higher than both the 2020 and 2025 targets by an appreciable margin, with the efficiency at rated power of 11kW also higher than both targets. In sum, the proposed integrated charger exceeds all 2020 targets and most of the 2025 targets whilst providing on-board charging capabilities, a bidirectional transformerless grid interface, enhancements to motor lifetime and traction mode efficiency increases.

VII. Conclusion

This paper demonstrated an integrated charger enabled by an LC filter with common mode voltage control with contactors to change between traction and charging modes,

TABLE V: Comparison of United States Department of Energy on-board charger technical targets at 500,000 units [2] and a single prototype of the proposed integrated charger.

Metrics	US DOE 2020	US DOE 2025	Single Prototype	Benefit
Cost ($/kW)	50	35	25.47	-49.1%[1] / -27.2%[2]
Specific power (kW/kg)	3	4	3.2	+6.67%[1] / -20%[2]
Power density (kW/L)	3.5	4.6	9	+257.4%[1] / +195.7%[2]
Efficiency	97%	98%	99.4%[3]	+2.4%[1] / +1.4%[2]

[1] Relative to 2020 US DOE target.
[2] Relative to 2025 US DOE target.
[3] Peak efficiency.

voltage sensors for the common mode voltage control and a common mode inductor to ensure 30mA leakage current compliance to permit transformerless three-phase charging. Variable frequency critical soft switching was employed to keep efficiency high and to make the LC filter small for traction applications. Bearing currents and shaft voltages are decreased by over 90%, which will result in increased motor lifespan. Peak efficiency of the inverter integrated charger was shown to be 99.4% and 98.4% at rated power of 11kW and traction mode saw an increase in efficiency of 0.6% over a standard 20kHz drive due to a decrease in PMSM core losses. When comparing to United States Department of Energy targets for mass production on-board chargers, a single prototype of the proposed integrated charger exceeds all metrics in 2020 and most in 2025, demonstrating a significant decrease in cost and increase in power density.

REFERENCES

[1] B. Bilgin, P. Magne, P. Malysz, Y. Yang, V. Pantelic, M. Preindl, A. Korobkine, W. Jiang, M. Lawford, and A. Emadi, "Making the Case for Electrified Transportation," *IEEE Transactions on Transportation Electrification*, vol. 1, no. 1, pp. 4–17, 2015.

[2] "US DRIVE Electrical and Electronics Technical Team Roadmap," United States Department of Energy, Tech. Rep. October, 2017. [Online]. Available: https://www.energy.gov/sites/prod/files/2017/11/f39/EETT Roadmap 10-27-17.pdf

[3] Y. Sun, M. Preindl, S. Sirouspour, and A. Emadi, "Unified Wide-Speed Sensorless Scheme Using Nonlinear Optimization for IPMSM Drives," *IEEE Transactions on Power Electronics*, vol. 32, no. 8, pp. 6308–6322, 2016.

[4] M. Eull, M. Mohamadian, D. Luedtke, and M. Preindl, "A Current Observer to Reduce the Sensor Count in Three-Phase PM Synchronous Machine Drives," *IEEE Transactions on Industry Applications*, vol. 55, no. 5, pp. 4780–4789, 2019.

[5] M. Eull and M. Preindl, "An Optimization-Based Reduced Sensor Virtual Flux Observer for PM Synchronous Machines," *IEEE Transactions on Industrial Electronics*, vol. 68, no. 5, pp. 4320–4330, 2021.

[6] M. Yilmaz and P. T. Krein, "Review of Battery Charger Topologies, Charging Power Levels, and Infrastructure for Plug-In Electric and Hybrid Vehicles," *IEEE Transactions on Power Electronics*, vol. 28, no. 5, pp. 2151–2169, 2013.

[7] Y. Du, X. Zhou, S. Bai, S. Lukic, and A. Huang, "Review of non-isolated bi-directional DC-DC converters for plug-in hybrid electric vehicle charge station application at municipal parking decks," in *Conference Proceedings - IEEE Applied Power Electronics Conference and Exposition - APEC*, no. 1, 2010, pp. 1145–1151.

[8] H. Tu, H. Feng, S. Srdic, and S. Lukic, "Extreme Fast Charging of Electric Vehicles: A Technology Overview," *IEEE Transactions on Transportation Electrification*, vol. 5, no. 4, pp. 861–878, 2019.

[9] J. Reimers, L. Dorn-Gomba, C. Mak, and A. Emadi, "Automotive Traction Inverters: Current Status and Future Trends," *IEEE Transactions on Vehicular Technology*, vol. 68, no. 4, pp. 3337–3350, 2019.

[10] S. Haghbin, S. Lundmark, M. Alaküla, and O. Carlson, "Grid-connected integrated battery chargers in vehicle applications: Review and new solution," *IEEE Transactions on Industrial Electronics*, vol. 60, no. 2, pp. 459–473, 2013.

[11] I. Subotic, N. Bodo, E. Levi, B. Dumnic, D. Milicevic, and V. Katic, "Overview of fast on-board integrated battery chargers for electric vehicles based on multiphase machines and power electronics," *IET Electric Power Applications*, vol. 10, no. 3, pp. 217–229, 2016.

[12] A. Khaligh and M. Dantonio, "Global Trends in High-Power On-Board Chargers for Electric Vehicles," *IEEE Transactions on Vehicular Technology*, vol. 68, no. 4, pp. 3306–3324, 2019.

[13] S. Loudot, B. Briane, O. Ploix, and A. Villeneuve, "Fast Charging Device for an Electric Vehicle. US 2012/028674.0 A1," 2012.

[14] I. Subotic, N. Bodo, and E. Levi, "An EV Drive-Train with Integrated Fast Charging Capability," *IEEE Transactions on Power Electronics*, vol. 31, no. 2, pp. 1461–1471, 2016.

[15] I. Subotic, N. Bodo, and E. Levi, "Integration of Six-Phase EV Drivetrains into Battery Charging Process with Direct Grid Connection," *IEEE Transactions on Energy Conversion*, vol. 32, no. 3, pp. 1012–1022, 2017.

[16] I. Subotic, N. Bodo, E. Levi, and M. Jones, "Onboard Integrated Battery Charger for EVs Using an Asymmetrical Nine-Phase Machine," *IEEE Transactions on Industrial Electronics*, vol. 62, no. 5, pp. 3285–3295, 2015.

[17] S. Q. Ali, D. Mascarella, G. Joos, and L. Tan, "Torque cancelation of integrated battery charger based on six-phase permanent magnet synchronous motor drives for electric vehicles," *IEEE Transactions on Transportation Electrification*, vol. 4, no. 2, pp. 344–354, 2018.

[18] Y. Xiao, C. Liu, and F. Yu, "An Effective Charging-Torque Elimination Method for Six-Phase Integrated On-Board EV Chargers," *IEEE Transactions on Power Electronics*, vol. 35, no. 3, pp. 2776–2786, 2020.

[19] S. Haghbin, S. Lundmark, M. Alaküla, and O. Carlson, "An isolated high-power integrated charger in electrified-vehicle applications," *IEEE Transactions on Vehicular Technology*, vol. 60, no. 9, pp. 4115–4126, 2011.

[20] S. Haghbin, K. Khan, S. Zhao, M. Alaküla, S. Lundmark, and O. Carlson, "An integrated 20-kW motor drive and isolated battery charger for plug-in vehicles," *IEEE Transactions on Power Electronics*, vol. 28, no. 8, pp. 4013–4029, 2013.

[21] W. Lhomme, P. Delarue, T. J. D. S. Moraes, N. K. Nguyen, E. Semail, K. Chen, and B. Silvestre, "Integrated Traction/Charge/Air Compression Supply Using Three-Phase Split-Windings Motor for Electric Vehicles," *IEEE Transactions on Power Electronics*, vol. 33, no. 11, pp. 10 003–10 012, 2018.

[22] S. Sharma, M. V. Aware, and A. Bhowate, "Integrated Battery Charger for EV by Using Three-Phase Induction Motor Stator Windings as Filter," *IEEE Transactions on Transportation Electrification*, vol. 6, no. 1, pp. 83–94, 2020.

[23] L. Solero, "Nonconventional on-board charger for electric vehicle propulsion batteries," *IEEE Transactions on Vehicular Technology*, vol. 50, no. 1, pp. 144–149, 2001.

[24] G. Pellegrino, E. Armando, and P. Guglielmi, "An integral battery charger with power factor correction for electric scooter," *IEEE Transactions on Power Electronics*, vol. 25, no. 3, pp. 751–759, 2010.

[25] C. Viana and P. W. Lehn, "A Drivetrain Integrated DC Fast Charger with Buck and Boost Functionality and Simultaneous Drive/Charge Capability," *IEEE Transactions on Transportation Electrification*, vol. 5, no. 4, pp. 903–911, 2019.

[26] C. Shi, Y. Tang, and A. Khaligh, "A single-phase integrated onboard battery charger using propulsion system for plug-in electric vehicles,"

IEEE Transactions on Vehicular Technology, vol. 66, no. 12, pp. 10 899–10 910, 2017.

[27] C. Shi and A. Khaligh, "A Two-Stage Three-Phase Integrated Charger for Electric Vehicles with Dual Cascaded Control Strategy," *IEEE Journal of Emerging and Selected Topics in Power Electronics*, vol. 6, no. 2, pp. 898–909, 2018.

[28] C. Shi, Y. Tang, and A. Khaligh, "A Three-Phase Integrated Onboard Charger for Plug-In Electric Vehicles," *IEEE Transactions on Power Electronics*, vol. 33, no. 6, pp. 4716–4725, 2018.

[29] Y. Xiao, C. Liu, and F. Yu, "An integrated on-board EV charger with safe charging operation for three-phase IPM Motor," *IEEE Transactions on Industrial Electronics*, vol. 66, no. 10, pp. 7551–7560, 2019.

[30] H.-C. Chang and C.-M. Liaw, "Development of a compact switched-reluctance motor drive for EV propulsion with voltage-boosting and PFC charging capabilities," *IEEE Transactions on Vehicular Technology*, vol. 58, no. 7, pp. 3198–3215, 2009.

[31] *Residual direct current detecting device (RDC-DD) to be used for mode 3 charging of electric vehicles*, IEC 62955:2018 Std., 2018.

[32] *Electric vehicle conductive charging system - Part 1: General requirements*, IEC 61851-1:2017 Std., 2017.

[33] *The IET Wiring Regulations 18th Edition*, BS 7671:2018 Std., 2018.

[34] W. Li, Y. Gu, H. Luo, W. Cui, X. He, and C. Xia, "Topology review and derivation methodology of single-phase transformerless photovoltaic inverters for leakage current suppression," *IEEE Transactions on Industrial Electronics*, vol. 62, no. 7, pp. 4537–4551, 2015.

[35] L. Zhou and M. Preindl, "Bidirectional Transformerless EV Charging System via Reconfiguration of 4x4 Drivetrain," in *2018 IEEE Energy Conversion Congress and Exposition, ECCE 2018*, 2018, pp. 3923–3927.

[36] I. Serban, "Power decoupling method for single-phase H-bridge inverters with no additional power electronics," *IEEE Transactions on Industrial Electronics*, vol. 62, no. 8, pp. 4805–4813, 2015.

[37] Y. Tang, W. Yao, P. C. Loh, and F. Blaabjerg, "Highly Reliable Transformerless Photovoltaic Inverters with Leakage Current and Pulsating Power Elimination," *IEEE Transactions on Industrial Electronics*, vol. 63, no. 2, pp. 1016–1026, 2016.

[38] M. Eull, W. Wang, L. Zhou, and M. Preindl, "Zero Sequence Voltage Control Enabling Transformerless Electric Vehicle Chargers," in *2021 IEEE Transportation Electrification Conference and Expo (ITEC)*, 2021.

[39] T. Hadden, J. W. Jiang, B. Bilgin, Y. Yang, A. Sathyan, H. Dadkhah, and A. Emadi, "A review of shaft voltages and bearing currents in EV and HEV motors," in *IECON Proceedings (Industrial Electronics Conference)*. IEEE, 2016, pp. 1578–1583.

[40] T. Plazenet, T. Boileau, C. Caironi, and B. Nahid-Mobarakeh, "A Comprehensive Study on Shaft Voltages and Bearing Currents in Rotating Machines," *IEEE Transactions on Industry Applications*, vol. 54, no. 4, pp. 3749–3759, 2018.

[41] T. Plazenet, T. Boileau, C. Caironi, and B. Nahid-Mobarakeh, "Influencing Parameters on Discharge Bearing Currents in Inverter-Fed Induction Motors," *IEEE Transactions on Energy Conversion*, vol. 8969, no. c, pp. 1–1, 2020.

[42] X. Shu, Y. Guo, W. Yang, K. Wei, Y. Zhu, and H. Zou, "A Detailed Reliability Study of the Motor System in Pure Electric Vans by the Approach of Fault Tree Analysis," *IEEE Access*, vol. 8, pp. 5295–5307, 2020.

[43] S. Chen, T. A. Lipo, and D. Fitzgerald, "Source of Induction Motor Bearing Currents Caused by PWM Inverters," *IEEE Transactions on Energy Conversion*, vol. 11, no. 1, pp. 25–32, 1996.

[44] H. Akagi and T. Doumoto, "An approach to eliminating high-frequency shaft voltage and ground leakage current from an inverter-driven motor," *IEEE Transactions on Industry Applications*, vol. 40, no. 4, pp. 1162–1169, 2004.

[45] H. Akagi and T. Doumoto, "A passive EMI filter for preventing high-frequency leakage current from flowing through the grounded inverter heat sink of an adjustable-speed motor drive system," *IEEE Transactions on Industry Applications*, vol. 41, no. 5, pp. 1215–1223, 2005.

[46] H. Akagi and S. Tamura, "A passive EMI filter for eliminating both bearing current and ground leakage current from an inverter-driven motor," *IEEE Transactions on Power Electronics*, vol. 21, no. 5, pp. 1459–1468, 2006.

[47] D. Hyypio, "Mitigation of bearing electro-erosion of inverter-fed motors through passive common-mode voltage suppression," *IEEE Transactions on Industry Applications*, vol. 41, no. 2, pp. 576–583, 2005.

[48] J. Kalaiselvi and S. Srinivas, "Bearing currents and shaft voltage reduction in dual-inverter-fed open-end winding induction motor with reduced CMV PWM methods," *IEEE Transactions on Industrial Electronics*, vol. 62, no. 1, pp. 144–152, 2015.

[49] H. Ayano, K. Murakami, and Y. Matsui, "A Novel Technique for Reducing Leakage Current by Application of Zero-Sequence Voltage," *IEEE Transactions on Industry Applications*, vol. 51, no. 4, pp. 3094–3100, 2015.

[50] L. De Sousa and H. Dogan, "Method of evaluating the zero-sequence inductance ratio for electrical machines," in *Proceedings of the 2011 14th European Conference on Power Electronics and Applications, EPE 2011*, 2011, pp. 1–10.

[51] Y. Wan, S. Cui, S. Wu, and L. Song, "Electromagnetic design and losses analysis of a high-speed permanent magnet synchronous motor with toroidal windings for pulsed alternator," *Energies*, vol. 11, no. 3, pp. 1–21, 2018.

[52] J. Biela, U. Badstuebner, and J. W. Kolar, "Impact of Power Density Maximization on Efficiency of DC – DC Converter Systems," *IEEE Transactions on Power Electronics*, vol. 24, no. 1, pp. 288–300, 2009.

[53] W. Chen, P. Rong, and Z. Lu, "Snubberless Bidirectional DC–DC Converter With New CLLC Resonant Tank Featuring Minimized Switching Loss," *IEEE Transactions on Industrial Electronics*, vol. 57, no. 9, pp. 3075–3086, 2009.

[54] D. Garcia, J. Valencia, and G. Hausman, "U.S. Department of Energy's 2016 transformer efficiency changes and impact on inrush current for low voltage dry-type transformers," Eaton Corporation, Tech. Rep., 2016.

[55] B. Agrawal, L. Zhou, A. Emadi, and M. Preindl, "Variable-Frequency Critical Soft-Switching of Wide-Bandgap Devices for Efficient High-Frequency Nonisolated DC-DC Converters," *IEEE Transactions on Vehicular Technology*, vol. 69, no. 6, pp. 6094–6106, 2020.

[56] L. Zhou and M. Preindl, "Variable-Switching Constant-Sampling Frequency Critical Soft Switching Model Predictive Control," *IEEE Transactions on Energy Conversion*, vol. 36, no. 2, pp. 1–1, 2021.

[57] M. Nymand, U. K. Madawala, M. A. E. Andersen, B. Carsten, and O. S. Seiersen, "Reducing AC-Winding Losses in High-Current High-Power Inductors," in *2009 35th Annual Conference of IEEE Industrial Electronics*. IEEE, 2009, pp. 777–781.

[58] R. Pittini, Z. Zhang, and M. A. Andersen, "High current planar magnetics for high efficiency bidirectional dc-dc converters for fuel cell applications," in *Conference Proceedings - IEEE Applied Power Electronics Conference and Exposition - APEC*. IEEE, 2014, pp. 2641–2648.

[59] R. Ramachandran and M. Nymand, "Experimental Demonstration of a 98.8% Efficient Isolated DC–DC GaN Converter," *IEEE Transactions on Industrial Electronics*, vol. 64, no. 11, pp. 9104–9113, 2017.

[60] M. Eull, M. Preindl, and A. Emadi, "A stochastic optimization technique for discrete DC capacitor bank design," in *2017 IEEE Transportation Electrification Conference and Expo (ITEC)*, 2017, pp. 9–14.

[61] M. Eull and M. Preindl, "Bidirectional three-level DC-DC converters: Sum-difference modeling and control," in *2017 IEEE Transportation Electrification Conference and Expo (ITEC)*, 2017, pp. 573–578.

[62] Q. Huang and A. Q. Huang, "Review of GaN Totem-Pole Bridgeless PFC," *CPSS Transactions on Power Electronics and Applications*, vol. 2, no. 3, pp. 187–196, 2017.

[63] F. M. Shah, H. M. Xiao, R. Li, M. Awais, G. Zhou, and G. T. Bitew, "Comparative performance evaluation of temperature dependent characteristics and power converter using GaN, SiC and Si power devices," in *Proceedings - 2018 IEEE 12th International Conference on Compatibility, Power Electronics and Power Engineering, CPE-POWERENG 2018*, vol. 2. IEEE, 2018, pp. 1–7.

[64] J. Yu, L. Li, J. Zhang, L. Pei, and L. Zhang, "Co-analysis of electromagnetic loss of the high speed PMSM driven by the PWM inverter," in *19th International Conference on Electrical Machines and Systems, ICEMS 2016*, no. 92. The Institute of Electrical Engineers of Japan, 2017, pp. 8–12.

[65] A. Muetze and E. G. Strangas, "The Useful Life of Inverter-Based Drive Bearings: Methods and Research Directions from Localized Maintenace to Prognosis," *IEEE Industry Applications Magazine*, no. 22, pp. 63–73, may 2016.

[66] J. Ahola, A. Muetze, M. Niemelä, and A. Romanenko, "Normalization-based approach to electric motor BVR related capacitances computation," *IEEE Transactions on Industry Applications*, vol. 55, no. 3, pp. 2770–2780, 2019.

[67] J. K. Park, T. R. Wellawatta, S. J. Choi, and J. Hur, "Mitigation Method of the Shaft Voltage According to Parasitic Capacitance of the PMSM," *IEEE Transactions on Industry Applications*, vol. 53, no. 5, pp. 4441–4449, 2017.

[68] S. Srdic and S. Lukic, "Toward Extreme Fast Charging: Challenges and Opportunities in Directly Connecting to Medium-Voltage Line," *IEEE Electrification Magazine*, vol. 7, no. 1, pp. 22–31, 2019.
[69] J. Rocabert, A. Luna, F. Blaabjerg, and P. Rodríguez, "Control of Power Converters in AC Microgrids," *IEEE Transactions on Power Electronics*, vol. 27, no. 11, pp. 4734–4749, 2012.
[70] M. Preindl, "High-performance selective and output filter techniques for sensorless direct position and speed estimation," *IEEE Transactions on Industrial Electronics*, vol. 67, no. 7, pp. 6000–6009, 2020.
[71] E. Hoevenaars and M. Hiller, "Conceptualization and Efficiency Review of Integrated Chargers Using Six-Phase Machines," *IEEE Transactions on Transportation Electrification*, vol. 7782, no. c, pp. 1–14, 2021.

Michael Eull (S'12) received the B.Eng.Mgt. and MASc degrees from McMaster University, Hamilton, ON, Canada and the PhD degree from Columbia University, New York, NY, USA, all in electrical engineering. He is currently a Research and Development Engineer in power electronics at the Power Networks Demonstration Centre, University of Strathclyde, United Kingdom and is serving as the Treasurer for the 2022 IEEE/AIAA ITEC+EATS conference. His research interests are in estimation and control of power electronics and motor drives for transportation electrification.

Liwei Zhou (S'15) received the B.E. and the M.E., both in Electrical Engineering, from Shandong University, Jinan, China in 2014 and 2017, respectively. He is currently working toward the Ph.D. degree in Motor Drives and Power Electronics Laboratory (MPLab), Columbia University, New York City, NY, USA. Since 2017, he has been a Graduate Research Assistant with MPLab. His current research interests include soft-switching techniques for modular power converter, model predictive control and other advanced control technologies, grid-connected converter and EV battery charging control, inductor design. He received the IEEE Energy Conversion Congress & Expo, 2018 Student Travel Award. He is also the co-recipient of the Best Student Paper Award of the IEEE Transportation Electrification Conference and Expo (ITEC), 2021.

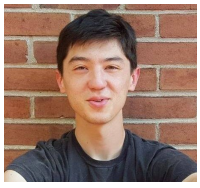

Matthew Jahnes (S'20) received the B.S. degree in electrical engineering from Rensselaer Polytechnic Institute in Troy, NY in 2017 and the M.S. degree in electrical engineering from Columbia University in New York, NY in 2019. He is currently working towards his Ph.D. at the Motor Drives and Power Electronics Laboratory (MPLab), Columbia University, New York, NY. His current research interests include novel power conversion topologies and high efficiency/high power density converter design.

Matthias Preindl (S'12-M'15-SM'18) received the B.Sc. degree in electrical engineering (*summa cum laude*) from the University of Padua, Italy, the M.Sc. degree in electrical engineering and information technology from ETH Zurich, Switzerland, and the Ph.D. degree in energy engineering from the University of Padua, in 2008, 2010, and 2014, respectively. He is currently Associate Professor of Power Electronic Systems in the Department of Electrical Engineering at Columbia University, USA. Prior to joining Columbia University in 2016, he was an R&D Engineer of Power Electronics and Drives at Leitwind AG, Italy (2010-2012), a Post Doctoral Research Associate with the McMaster Institute for Automotive Research and Technology, McMaster University, Hamilton, ON, Canada (2014-2015), and a Sessional Professor in the Department of Electrical and Computer Engineering, McMaster University (2015). He serves as the area editor of vehicular electronics and systems at the IEEE Transactions on Vehicular Technology and as the general chair of the 2022 IEEE/AIAA ITEC+EATS. He received several awards and honors including the Horiba Awards Honorable Mention (Japan, 2019), the Futura Foundation Award (Italy, 2017), the NSF CAREER Award (USA, 2017), and he is the co-recipient of several best paper and presentation recognitions including the 2019 IEEE Transactions on Industrial Electronics best paper award.